ACS APPLIED NANO MATERIALS

www.acsanm.org Article

Micron-Sized Nanostructured Si−C Composites for High-Performance Li-Ion Battery Anodes

Joseph F. Wild, Yihan Li, Yeshiyuan Zhou, Wenbo Bao, Aishwarya Gujarathi, Ruiwen Zhang, Yuxuan Yang, Tao Hu, Taizhi Jiang, Yihong Chen, and Yuan Yang*

Cite This: https://doi.org/10.1021/acsanm.5c03801 Read Online

ACCESS | Metrics & More | Article Recommendations | Supporting Information

ABSTRACT: Silicon−carbon composite materials offer an attractive and realistic pathway to lithium-ion batteries with higher energy density. Here, a scalable chemical vapor deposition (CVD) process is used to form micron-sized Si−C composites with uniform few-atomic-layer Si on nanoporous carbon. We find that the optimal deposition temperatures are 450−525 °C. The ultrathin Si layer successfully releases stress in the micron-sized particles, while the small pores eliminate the formation of excessive amounts of solid electrolyte interphase, as validated by elemental mapping. Therefore, the resulting Si−C composites demonstrate a high specific capacity exceeding 1400 mAh/g, stable cycling with a decay rate of <5%/100 cycles in the half cell, an initial Coulombic efficiency of 85.2%, and excellent rate capabilities such as 84% retention at 4C. Moreover, the material demonstrates excellent air and water stability, allowing for similar electrode casting and preparation methods as graphite. The corresponding $LiNi_{0.92}Mn_{0.02}Co_{0.06}O_2$/Si−C full cells show stable cycling with 84% capacity retention over 200 cycles, which is attractive for high-energy-density lithium-ion batteries and compares favorably to other silicon-based anodes in terms of both performance and scalability.

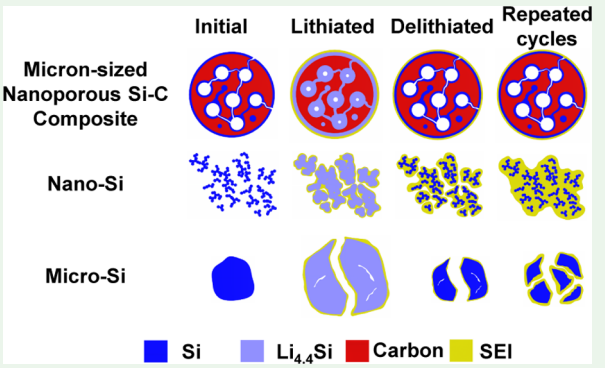

KEYWORDS: *Si anode, nanoporous, Li-ion batteries, chemical vapor deposition, Si−C composite*

1. INTRODUCTION

Lithium-ion batteries are essential to modern life and a sustainable future.[1−3] The technology is at the intersection of allowing for clean electrification of the transport and energy industries. Compared to alternative energy storage technologies such as Zn−air,[4] hybrid-ion,[5] ammonium-ion,[6,7] microbial fuel cell,[8] and supercapacitors,[9] Li-ion batteries offer a good balance of high energy density, rechargeability, and scalability for mobile and grid applications. However, materials with higher specific capacities are desired for wider adoption, especially for satisfying the needs of electric vehicles. Moreover, advanced materials that can be readily produced and seamlessly integrated into existing and planned production lines stand the best chance of accelerating electrification in the near term.[10−16]

Over the past decade, steady improvements have been made to Li-ion battery cathode materials, notably in increasing the Ni content in $LiNi_xMn_yCo_{1-x-y}O_2$ and $LiNi_xCo_yAl_{1-x-y}O_2$.[17] However, significant improvements at the cell level require improvements to both the anode and cathode, but the use of graphite as the anode material has remained mostly stagnant in commercial Li-ion batteries since its inception. Advanced anode materials offer a direct pathway to much greater specific capacities and have demonstrated workable solutions, albeit often at a prohibitively expensive production route.[18−20] While graphite does offer a modest specific capacity of 372 mAh/g, it is less than 1/10 of the specific capacity of Si at 4200 mAh/g.[21] Moreover, silicon-based anodes present a simple route to production due to their ability to use liquid electrolyte and be cast onto the current collectors like graphite; however, fundamental issues relating to cracking, volume expansion, low lithium diffusivity, and poor solid electrolyte interphase (SEI) formation have so far plagued cycle life and their widespread adoption.[11,22,23]

Nanostructures have been widely explored to address the Si volume expansion issue by keeping Si size below the critical fracture lengths (e.g., 240−360 nm for pillars, 150−200 nm for crystalline particles, and up to 870 nm for amorphous Si),[24,25] but the large surface area causes low initial Coulombic efficiency and side reactions.[14,26−29] Nanomaterials also have

Received: August 15, 2025
Revised: October 26, 2025
Accepted: October 28, 2025

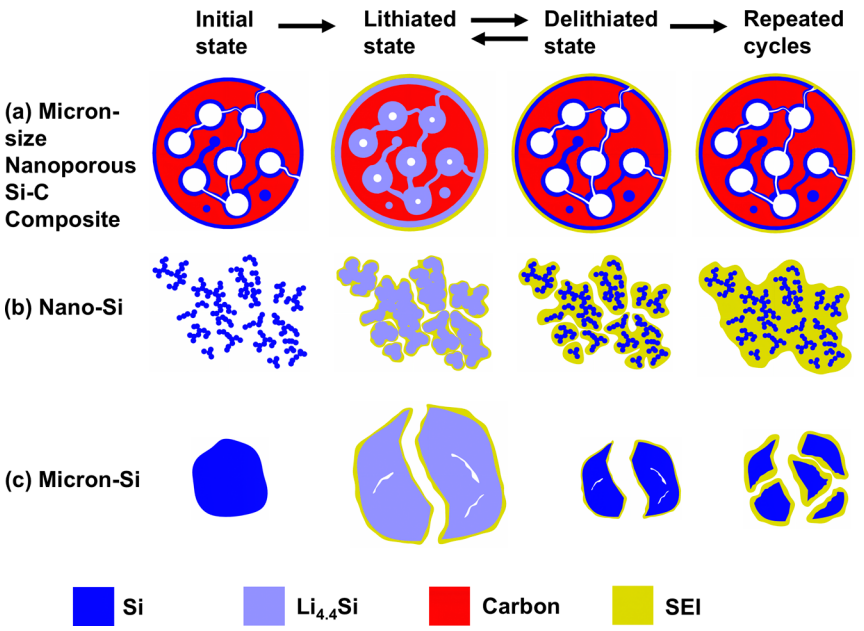

Figure 1. Schematic of the design principle and cycling behavior of micron-sized nanoporous Si−C composites (mn-Si−C) compared to traditional nano- and micron-Si. (a) mn-Si−C shows large pore volume and high lithium diffusivity via a carbon scaffold with thin Si coating. The large particle size minimizes outer exposed surface area and increases tap density, while the small pore size restricts SEI formation to the outer surface. In contrast, the large exposed surface area of the pure nano-Si (b) leads to excess decomposition products, while the micron-Si (c) leads to particle cracking due to being larger than the critical fracture length.

low tapping density, which compromises energy density in full cells.[30−32]

Here, we developed nanostructured Si−C composite materials for high-performance Li-ion battery anodes to address these issues. In general, few-atomic-layer amorphous Si is deposited onto micron-sized particles of nanoporous carbon using a scalable chemical vapor deposition (CVD) process.[33,34] Optimized deposition conditions were used to achieve a highly uniform distribution of silicon both among particles and within the particles. The resulting Si−C composite has a specific capacity exceeding 1400 mAh/g and an exceptional rate performance. It also leads to steady cycling in NMC/Si−C full cells with a capacity retention of 84%/200 cycles. In addition, the material is simple to synthesize and maintains good compatibility with a water-based solvent and open-air casting.

2. MATERIALS AND METHODS

2.1. Material Synthesis and Deposition. Nanoporous carbon powder ($D_{50} \approx 6.1$ μm, SSA ≈ 1700 m^2/g, pore diameter ≈ 1.85 nm, pore volume ≈ 0.80 cm^3/g) is provided by Gotion Inc., which is made by high-temperature carbonization of an asphalt-based precursor. The nanoporous carbon powder exhibits an amorphous structure with nanoscale porosity, as confirmed by Raman spectroscopy, TEM imaging (Figure S3), and X-ray diffraction (Figure S4), consistent with its high surface area of ~ 1700 m^2 g^{-1} (Table S1).

The Si−C composites were synthesized via chemical vapor deposition (CVD) in a rotating quartz tube furnace. Prior to deposition, the furnace was flushed with N_2 gas and heated to 485 °C. After thermal stabilization, a 2% SiH_4/N_2 gas mixture was introduced for 100 min at 0.8 atm with a 150 sccm total flow rate and a 5 rpm rotation rate, resulting in Si loadings of ∼43 wt % as determined by thermogravimetric analysis (TGA, TA Instruments, Q50). All depositions were conducted using a closed, continuously purged quartz tube furnace system with safety interlocks (Supporting Information Figure S1), and the 2% SiH_4/N_2 mixture was handled under numerous outlined safety protocols. Extreme caution should be paid to handling SiH_4, even when diluted to 2%.

2.2. Material Characterization. Surface area and pore structure were evaluated by Brunauer−Emmett−Teller (BET) analysis and Barrett−Joyner−Halenda (BJH) pore size distribution using a Micromeritics ASAP 2020 instrument. Raman spectra were collected with an Explora Plus MicroRaman Spectrometer (Confocal Raman Microscope). SEM and FIB-EDS mapping were performed on an FEI Helios Nanolab 660 FIB-SEM equipped with an Oxford EDX detector. Pore filling and Si uniformity were assessed through cross-sectional imaging and MATLAB-based image quantification. TEM was conducted on an FEI TALOS F200X at 200 kV for morphological assessment. TGA was performed in air at 10 °C/min from room temperature to 1000 °C.

2.3. Electrode Fabrication and Cell Assembly. Materials: Cathodes used $LiNi_{0.92}Mn_{0.02}Co_{0.06}O_2$ (NMC92) provided by ORI with Kynar 761 poly(vinylidene fluoride) (PVdF) binder (Arkema) and super C65 carbon black (MSE Supplies LLC). *N*-methylpyrrolidone (NMP) was the solvent (Sigma-Aldrich). For anodes, the nanoporous carbon was provided by Gotion, Inc., with carboxymethyl cellulose (CMC) (MTI), poly(acrylic acid) (PAA) (Sigma-Aldrich), carbon nanotubes (CNT) (Tuball), and super C65 carbon black. The separator used was a Celgard 2325. LP40 conventional electrolyte 1 M lithium hexafluorophosphate ($LiPF_6$) in ethylene carbonate and diethyl carbonate (EC/DEC = 1:1) was provided by Gotion Inc. Vinylene carbonate (VC) (Gotion, Inc.) was used to prepare the electrolyte.

For half-cell preparation, Si−C powder was mixed with poly(acrylic acid), carboxymethyl cellulose, carbon nanotubes, and carbon black in a mass ratio of 75:7.5:7.5:1:9 using DI water as a solvent. The slurry was mixed in a Thinky ARM-310 planetary mixer and cast onto 10 μm Cu foil by using a doctor blade with a 200 μm gap. After drying under vacuum at 150 °C for 2 h, electrodes were punched into 15 mm discs and assembled into CR2032 coin cells with Li metal as the counter electrode in an argon-filled glovebox (H_2O, $O_2 < 0.1$ ppm). The electrolyte used was 1 M $LiPF_6$ in EC/DEC (1:1 wt %) with 3 wt % vinylene carbonate (VC). Celgard 2325 (25 μm) was used as the separator, and 40 μL of electrolyte was added per side.

https://doi.org/10.1021/acsanm.5c03801
ACS Appl. Nano Mater. XXXX, XXX, XXX−XXX

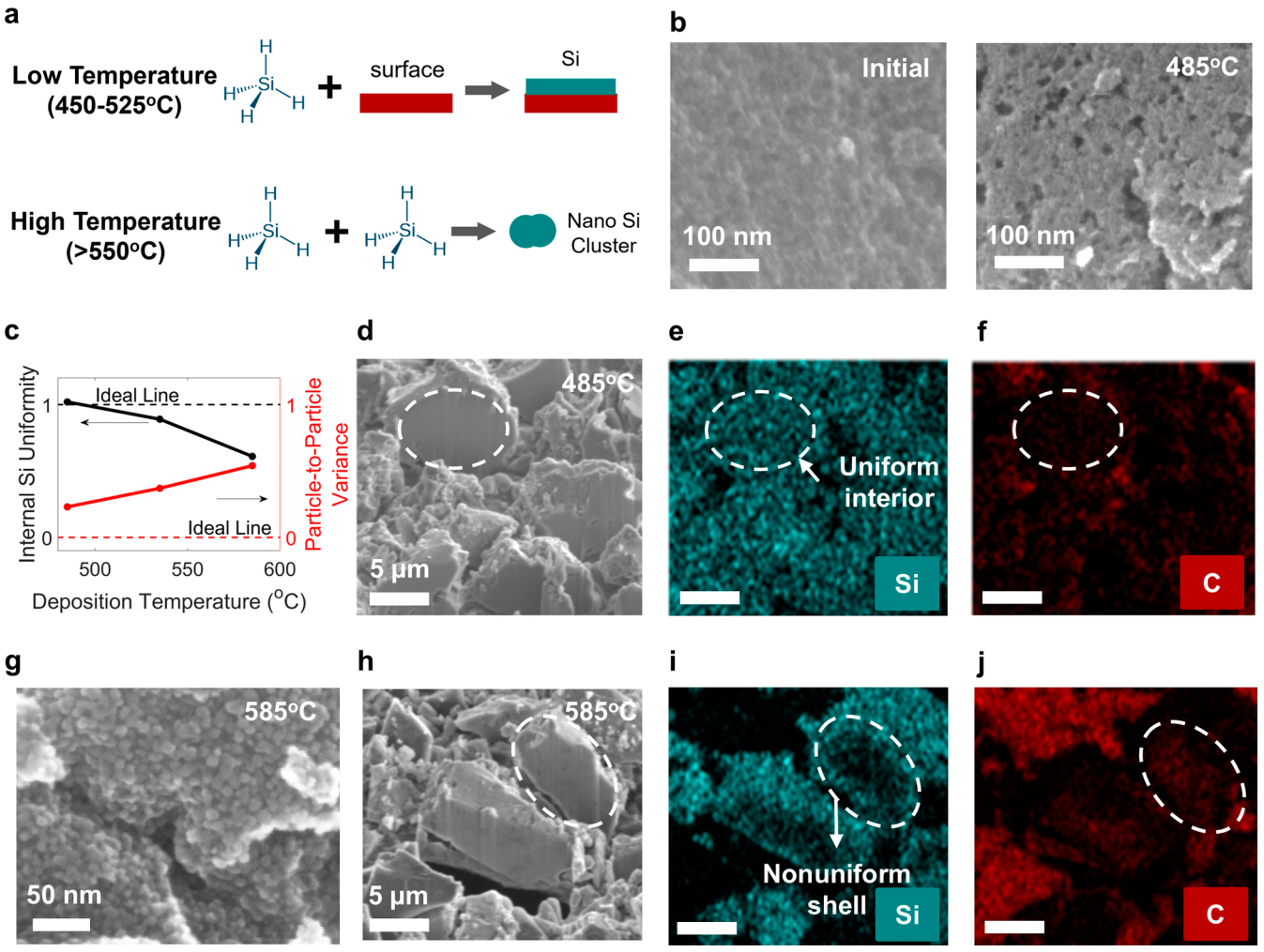

Figure 2. (a) Schematic illustrating the two dominant decomposition mechanisms of Si during chemical vapor deposition for the conditions studied. (b) SEM images of the surface of initial nanoporous carbon (left) and Si−C powders after a 485 °C deposition (right), covered by a thin Si layer. (c) Results of deposition uniformity vs temperature. Other deposition parameters are 0.8 atm total gas pressure, 150 ccm gas flow rate, and 5 rpm rotation rate. Both Si uniformity and particle-to-particle variance show better results at lower temperatures. (d) An SEM image, (e) EDS mapping of Si, and (f) EDS mapping of C of the Si−C composite with Si deposited at 485 °C. (g) SEM images of the surface of Si−C powders for a 585 °C deposition, showing a completely blocked surface of nano-Si whereby Si cannot deposit internally, and an undesired shell of Si is formed. (h−j) Images for SEM, Si EDS, and C EDS, respectively, for the 585 °C deposition in (g).

Full cells used a cathode of $LiNi_{0.92}Mn_{0.02}Co_{0.06}O_2$ (NMC-92) with a composition of NMC/PVDF/carbon black = 85:7.5:7.5 and 1.5× *N*-methylpyrrolidone as solvent. The slurry was cast on 16 μm Al foil using a 250 μm gap and dried at 110 °C. Discs of 16 mm in size were punched and matched with Si−C anodes (N/P = 1.15) for full cell assembly. The electrolyte and separator were the same as those for half cells.

2.4. Electrochemical Testing. Galvanostatic cycling was conducted using a Landt battery tester at room temperature (20 ± 3 °C) in an open laboratory. Half-cells were cycled at C/10 and C/5 for formation, followed by C/3 for cycling, unless otherwise stated. Here, 1C corresponds to 1400 mA g^{-1} based on the cycling capacity. The Si−C areal capacity was 2.0 ± 0.2 mAh cm^{-2}. This corresponds to an active material loading of ∼ 1.4 ± 0.1 mg cm^{-2}. The half-cell voltage window was 0.01−1.00 V. Full cells were cycled with C/10 formation followed by C/3 long-term cycling, with constant-voltage charging cutoffs at C/50 (formation) and C/20 (cycling). The full cell voltage window was 2.00−4.25 V.

3. MATERIAL DESIGN

Figure 1 illustrates the design principles of the micron-sized nanoporous Si−C composite (mn-Si−C) anodes compared to conventional nano- and micron-sized Si electrodes.[23] By depositing silicon within the interior of nanoporous micrometer-sized carbon particles, the design (1) effectively isolates silicon from direct electrolyte contact since the ultrasmall pores limit electrolyte infiltration, while large micrometer-sized particles reduce the ratio of surface area to enclosed volume. Specifically, the nanoporous carbon particles initially have pore sizes of ∼ 1.85 nm (as measured by BET). By depositing Si until pores become smaller than electrolyte molecule widths (EC ∼ 0.8 nm, DEC ∼ 0.9 nm, VC ∼ 0.8 nm), we effectively block electrolyte infiltration and limit SEI formation strictly to particle exteriors. (2) The thin silicon layer prevents fracture and pulverization during cycling, while the micron-scale particle size ensures a high tapping density of 0.56 g/cm^3. (3) The carbon scaffold has the benefit of enhancing both electrical conductivity and lithium-ion diffusivity throughout the composite, similar to other conductive frameworks.[10,26,35−39] In contrast, the large exposed surface area of nano-Si leads to excessive SEI growth, while micron-Si

https://doi.org/10.1021/acsanm.5c03801
ACS Appl. Nano Mater. XXXX, XXX, XXX−XXX

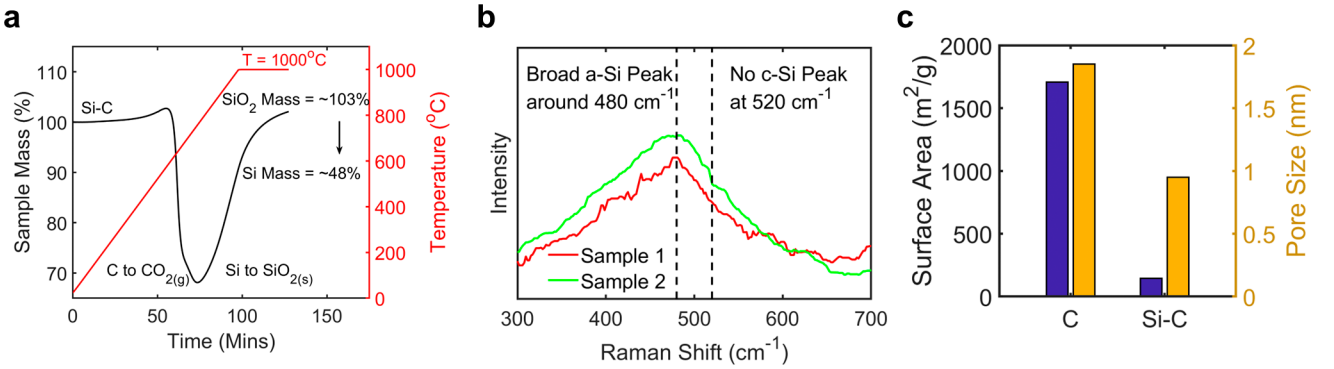

Figure 3. (a) Thermogravimetric analysis (TGA) used to determine the Si wt % of Si−C composite materials after deposition. (b) Raman spectroscopy of the as-synthesized Si−C composite powders. No sharp peak is visible at 520 cm^{-1}, indicating no crystalline Si in the material. (c) Brunauer−Emmett−Teller (BET) analysis for determining the surface of the micron-sized nanoporous carbon before and after Si deposition at 485 °C.

inevitably fractures and disintegrates upon repeated cycling (Figure 1b,c).

In this paper, we use nanoporous carbon derived from organic plant matter, which is naturally abundant.[40] It features 1−3 nm pores and a large surface area of 1600−1800 m^2/g. With a median particle diameter (D50) of 5−7 μm (Table S1), this design of small pores and large particles minimizes exposed external surface area prone to SEI formation while maintaining excellent rate performance. The synthesis process of mn-Si−C involves loading nanoporous carbon into a rotary tube furnace and using 2% SiH_4 in N_2 gas to deposit amorphous silicon. By carefully controlling deposition parameters such as temperature, pressure, and duration, a uniform few-atomic-layer Si coating is achieved, which reduces pore size to <1 nm, and the surface area is reduced to 144 m^2/g from the initial nanoporous carbon (setup details in Supporting Information Section S1). Compared to prior approaches involving Si nanoparticles or Si@graphite blends,[12,23,29] this work achieves uniform, few-atomic-layer Si coatings via CVD inside micron-sized porous carbon, enabling high performance and production compatibility with minimal SEI formation.

4. RESULTS

4.1. Synthesis of the Si−C Composite. Over 150 tube furnace depositions were performed to test various operating conditions to achieve optimal deposition conditions for particle-to-particle and interparticle uniformity.[41] A combination of scanning electron microscopy (SEM), energy dispersive spectroscopy (EDS), and focused ion-beam (FIB) allowed deposited particles to be cut in half such that the uniformity of Si inside the particles could be assessed, as shown in Figures S5 and S6. A MATLAB script was written to quantify this uniformity, with further details given in Supporting Information Section S3.

We found that temperature is the most critical parameter to achieve a uniform deposition of Si inside nanoporous carbon, with the optimal deposition temperatures being 450−525 °C (Figure 2a),[42] and 485 °C is used as a standard temperature in this study. At 485 °C, after 100 min of deposition, we obtained Si−C composites with a Si content of 41−45 wt %, as validated by thermogravimetric analysis (TGA) measurements (Figure 3a).

SEM imaging shows that the particle surface is covered by a thin layer of Si, indicating little deposition of Si outside the carbon particles (Figure 2b). Moreover, cross-sectional FIB-EDS mapping shows that Si is distributed uniformly inside of multiple particles (Figure 2d−f). Further quantitative EDS count analysis shows that the Si intensity is more uniform along the radius direction at lower temperatures (Figure 2c). The internal Si uniformity is defined as the Si EDS intensity at the center core of the cut particle compared to the outermost shell, while the variance is the uniformity statistics over 6−10 particles (Figure S6).

In contrast, when the temperature increased to 585 °C, an obvious granular Si layer was observed on the carbon surface in SEM imaging (Figure 2g). Moreover, cross-sectional FIB-EDS mapping shows that Si counts decrease substantially from the surface to the center of these micrometer-sized particles (Figure 2h−j). Particularly, Figure 2i further shows a clear gradient of the Si concentration along the radial direction at 585 °C.

The significant temperature-dependent Si deposition originates from the competition between SiH_4 decomposition kinetics and SiH_4 diffusion in nanoporous carbon. The diffusivity of SiH_4 at 485 °C is $\sim 4.5 \times 10^{-7}$ m^2/s in such nanoporous carbon, indicating that it takes only $\sim$ 10 μs to diffuse into the core of a nanoporous particle with a radius of 3 μm.[41] On the other hand, the deposition rate of Si on a flat substrate is 0.5 nm/min at 485 °C with 2% SiH_4. Therefore, the diffusion is fast enough to realize uniform deposition of Si across the entire micron-sized carbon particles. In contrast, the deposition rate of Si on a flat substrate reaches >50 nm/min at 585 °C with 2% SiH_4, which outpaces SiH_4 diffusion and closes the outer pores, leading to the strong gradient of Si distribution inside a particle. Temperatures below 450 °C result in sluggish decomposition kinetics and excessive deposition times, which are not practical for Si deposition.

Besides temperature, the other deposition parameters used are 0.8 atm pressure, 150 ccm of total gas, 200 mg of carbon loading, and 5 rpm rotation rate of the quartz tube. The deposition time was used to accurately tune the Si wt %, while TGA was used to determine Si wt % based on the assumption that all carbon is oxidized to CO_2 and Si is fully converted to SiO_2, which is validated by the white color of the final product (Figure S8). Typically, 43 ± 2% Si wt % was targeted, requiring $\sim$ 100 min of deposition (Figure 3a). Deposited Si was confirmed to be solely amorphous, evidenced by the broad peak at 480 cm^{-1} and the absence of the crystalline Si peak at 520 cm^{-1} (Figure 3b) from Raman Spectroscopy and a broad

https://doi.org/10.1021/acsanm.5c03801
ACS Appl. Nano Mater. XXXX, XXX, XXX−XXX

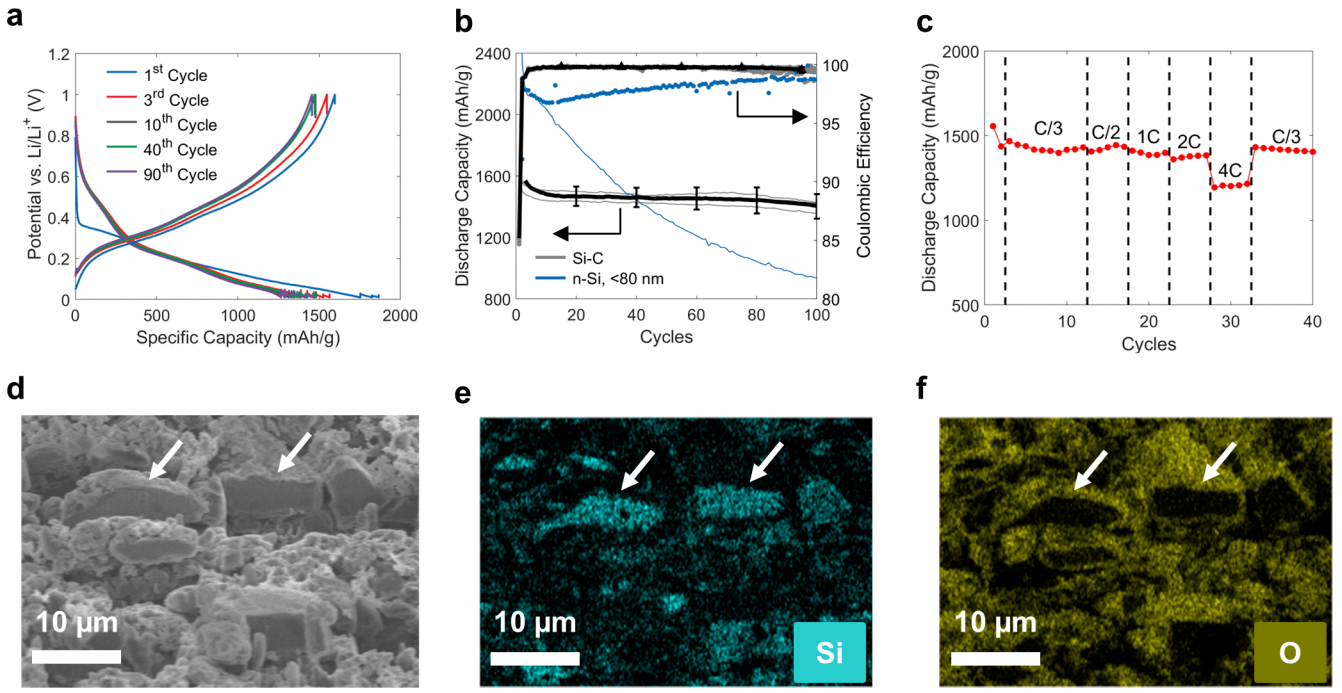

Figure 4. Si−C/Li half-cell cycling results. (a) Potential charge and discharge curves for the Si−C composite materials vs Li/Li^+. (b) Discharge capacity and cycling efficiency vs cycle number. Gray points represent individual data, with the thicker line indicating the mean. Error bars are shown every 20th cycle and represent $\pm 2\sigma$. (c) Rate performance when cycled at C/3, C/2, 1C, 2C, and 4C. Note: only one representative cell was tested for C-rate performance; error bars are therefore not shown. (d) Post-mortem SEM-FIB of the cycled half cells after 100 cycles. Visibly flat surfaces indicate those which have been cut and exposed by the focused ion beam (e,f) are Si and O, respectively, EDS mappings for (d), indicating pristine Si−C remaining on the interior with little O present, and hence SEI, which was confirmed to still be amorphous Si only via Raman spectroscopy in Figure S12. The EDS mapping for C is shown in Figure S7.

low-angle background characteristic from XRD images (Figure S4), confirming the amorphous structure of the as-synthesized Si−C composites.[43] Amorphous Si is preferred over crystalline Si since amorphous Si has faster Li diffusion kinetics, and it is more resilient to fracture upon lithiation.[25] Brunauer−Emmett−Teller (BET) analysis showed that the surface area of the as-synthesized Si−C material was 144 m^2/g for 43 wt % Si after a 485 °C deposition, down from 1706 m^2/g in the initial nanoporous carbon in Figure 3c. The adsorption average pore diameter correspondingly decreased from 1.85 to 0.95 nm (Figure 3c). This reduction suggests a Si coating thickness of ∼ 0.45 nm per side, which corresponds to approximately 2−3 atomic layers of silicon. This result supports that Si fills pores throughout the carbon and that the open pores on the carbon surface are so small that the electrolyte has difficulty penetrating the interior of carbon particles once a few-nm SEI layer is formed.

4.2. Electrochemical Performance. To understand the electrochemical performance of as-prepared Si−C composites, we prepared Si−C/Li half cells in the coin cell configuration. The Si−C electrode was mixed with poly(acrylic acid), carboxymethyl cellulose, carbon nanotubes, and carbon black at a mass ratio of 75:7.5:7.5:1:9 with deionized water as the solvent.[44,45] The electrolyte was 1 M $LiPF_6$ in EC/DEC (1:1 in weight) with 3 wt % vinylene carbonate.[46] The areal capacity of the Si−C electrode was 2.0 ± 0.2 mAh/cm^2 in half-cells. While this is slightly below the industrial target of 3−5 mAh/cm^2, testing of higher loading electrodes and addressing the associated challenges will be pursued in future work.

Figure 4a shows the voltage profile of a representative Si−C composite electrode. The voltage profile resembles that of amorphous silicon since amorphous carbon only has a specific capacity of ∼ 190 mAh/g (Figure S9). With three tested cells in Figure 4b, at C/10 (1C = 1400 mA/g), the initial specific capacity is 1843 ± 70 mAh/g ($\pm 2\sigma$) during lithiation and 1570 ± 70 mAh/g during delithiation, representing an attractive initial Coulombic efficiency (ICE) of 85.2 ± 0.7%, representing high cell-to-cell consistency. The ICE of 85.2% is somewhat lower than the best-reported values (91%−92%), which we attribute to the larger exposed Si surface area and nonoptimized electrode formulations in this work.[47] The specific capacity aligns closely with the expected value (∼1850 mAh g^{-1}) based on 44 wt % Si, which includes ∼ 90 mAh/g from the carbon scaffold, based on the fact that the reversible capacity of nanoporous carbon is ∼ 190 mAh/g (Figure S9). This indicates that most Si is active during cycling. All specific capacities are reported based on the total Si−C active material mass, excluding binder and conductive additives.

The cycle life testing was performed at C/3 after two formation cycles at C/10 and C/5 each. In three representative cells, the first delithiation capacity of C/3 is 1512 ± 73 mAh/g. The capacity fades between the 10th and 90th cycles are 4.4%, 1.5%, and 4.5%, which are significantly lower than the nano-Si degradation of 51.6% starting from 2036 mAh/g over the same range. Moreover, after 100 cycles, we do not see either cracks of the Si−C composite anode nor the formation of a large quantity of SEI in SEM-FIB-EDS characterizations. The latter is evidenced by no O or F signal inside Si−C particles (Figure 4d−f). It should be noted that we do see faster capacity fading after 100 cycles (Figure S9c), which can be attributed to (1) increasing impedance on the lithium metal anode due to thicker SEI and (2) capacity fading in the Si electrode.

https://doi.org/10.1021/acsanm.5c03801
ACS Appl. Nano Mater. XXXX, XXX, XXX−XXX

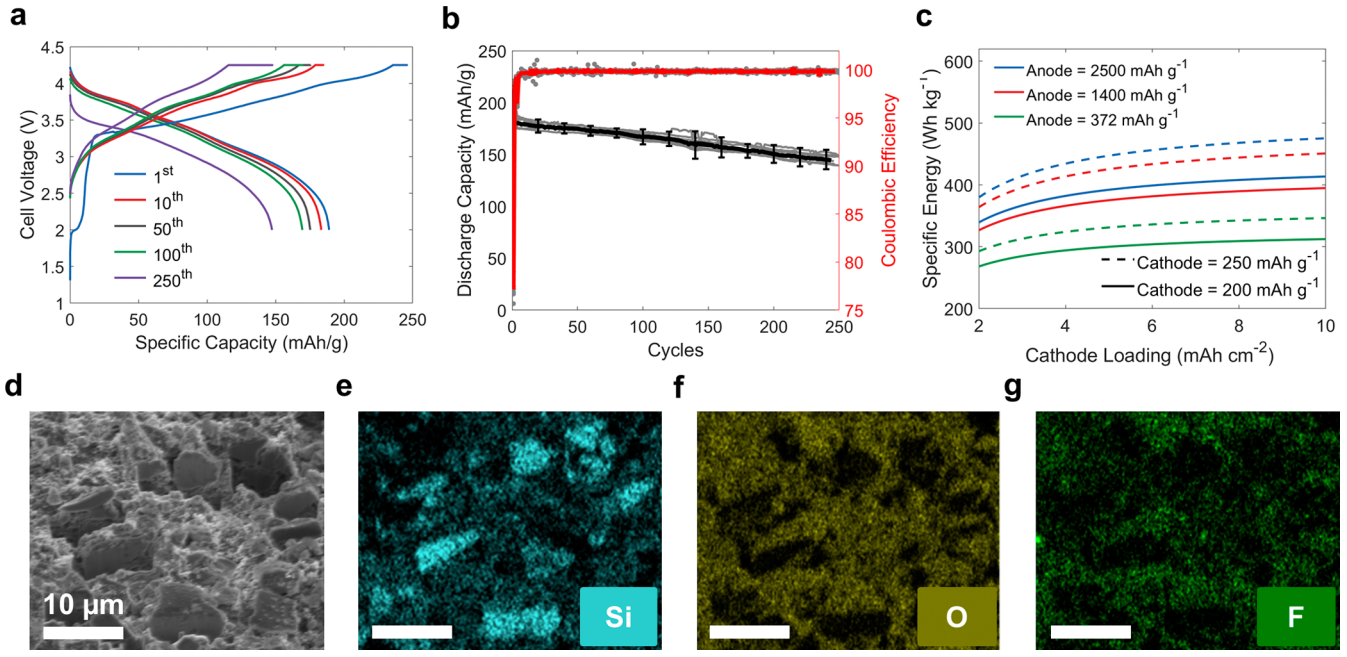

Figure 5. Si−C/NMC full cell cycling results. (a) Voltage charge and discharge curves for the Si−C/NMC full cells. (b) Discharge capacity and cycling efficiency vs cycle number. Gray points represent individual data, with the thicker line indicating the mean. Error bars are shown every 20th cycle and represent ± 2σ. Further cycling is shown in Figure S11. (c) Specific energy vs cathode loading for theoretical pouch cells and combinations of anode and cathode specific capacities. When the cathode capacity is much lower than the anode, it is relatively more advantageous to increase the cathode capacity to increase cell-specific energy. (d) Post-mortem SEM-FIB of the cycled cells after 610 cycles, again indicating pristine Si−C remaining on the interior with the EDS Si mapping (e) and no evidence of internal SEI formation from the lack of internal O and F in (f,g), respectively.

To understand the power capability of the Si−C composite, C-rate testing was performed by progressively cycling 5 times at C/2, 1C, 2C, and 4C after 10 initial cycles at C/3. The average discharge capacity for each of these 5 cycles was 1426, 1396, 1375, and 1205 mAh, respectively (Figure 4c). This demonstrates that the Si−C composites are able to retain over 84% of their capacity at a 4C discharge, thereby making them suitable for power applications. After these progressive cycles, the capacity returned to 1432 mAh/g at C/3. It should be noted that higher current rates (e.g., 4−10 C) are needed for full evaluation of the as-developed Si−C composite, which will be reported in future work.

To further evaluate the performance of as-prepared Si−C composites in full cells, we assembled Si−C/Li-$Ni_{0.92}Mn_{0.02}Co_{0.06}O_2$ (NMC) cells. The NMC electrode has a mass ratio composition of NMC, poly(vinylidene fluoride), and carbon black = 85:7.5:7.5. It shows an excellent performance of 220 mAh/g during the first discharge in NMC/Li half cells (Figure S10). An N/P ratio of 1.15 ± 0.01 was used, and the mass loading of the cathode is 1.9 ± 0.2 mAh/cm^2. All cells were cycled between 2.00 and 4.25 V. The first three cycles were at C/10 with a constant voltage (CV) charge step until C/50, while the remaining cycles were at C/3 with a CV charge step until C/20.

In Figure 5a,b, seven representative cells showed a mean initial Coulombic efficiency of 77.3 ± 2.2% (±2σ), a first discharge capacity of 190.1 ± 5.1 mAh/g at C/10, a first discharge capacity of 180.0 ± 9.0 mAh/g at C/3, and a decay of 16.0 ± 3.7% over the first 200 cycles. Such capacity retention in full cells is attractive for further developing Si−C composite anodes with long cycle life and compares favorably with other recent Si-anode studies (Table S3).[12,30,48−59] Extended cycling data are shown in Figure S11, where the Si−C/NMC full cells retain ∼ 62% of their capacity after 500 cycles, further confirming the favorable long-term stability of the composite anode. The short plateau near 2 V in the first charge (Figure 5a) arises from initial side reactions at the anode, such as Cu oxide reduction and electrolyte/humidity cleanup, and disappears in subsequent cycles.

The decay in the full cell could stem from both the Si/C anode and NMC cathode. NMC92/Li half-cell data (Figure S10) show a ∼15% capacity fade over 100 cycles (220 mAh g^{-1} to 188 mAh g^{-1}), which is faster than the decay observed in the full cells. This difference could originate from one of the following two mechanisms: (1) degradation at the lithium metal counter electrode, such as dendrite formation and electrolyte consumption. (2) NMC cathode cycles over a shallower state-of-charge range in full cells (∼180 mAh g^{-1} in full cells vs ∼220 mAh g^{-1} in half cells). As a result, the degradation in full cells is less.

The half-cell and full-cell cycling performance at 485 °C is much better than corresponding cells at 535 and 585 °C (Figure S13). For example, in full cells, the initial discharge capacity at 535 and 585 °C is only 136 and 125 mAh/g NMC at C/3, respectively, due to the lower Coulombic efficiency in these materials. The full-cell specific capacity also quickly decreases from 119 in cycle 5 to 103 mAh/g in cycle 80 at 535 °C, and from 92 to 86 mAh/g after 80 cycles at 585 °C (Figure S13).

To understand the decay mechanism, we used SEM-FIB-EDS to analyze the Si−C anode after the capacity decays to 60% after 610 cycles, as shown in Figure 5d−g. The results showed pristine Si−C and no evidence of particle cracking or island formation, indicating that the decay mechanism is not due to cracks in the Si−C composite, highlighting its advantage over micron-sized Si particles. Moreover, EDS mapping shows

https://doi.org/10.1021/acsanm.5c03801
ACS Appl. Nano Mater. XXXX, XXX, XXX−XXX

that elements of SEI, such as O and F, are mainly outside particles, indicating that SEI did not meaningfully form in the nanoporous interior. Post-mortem analysis via SEM-FIB-EDS mapping (Figures 4f and 5f,g) further confirmed this hypothesis, showing no significant penetration of SEI products (e.g., O and F) into the nanoporous interior, thus validating our design principle of using nanoporous materials to regulate SEI formation exclusively on the outside surface, instead of the inside surface, which is protected from the electrolyte via the nanopores.

The SEI chemistry on Si−C composite appears to be similar to pure Si nanoparticles (NPSi)-based electrodes after 5 cycles, as shown in Figure S14. Both electrodes form SEI layers consisting of LiF, Li−CO_2^-, and $Li_xP_yOF_z$. The Si−C electrodes exhibit a higher LiF fraction with a moderate amount of organic carbonate, illustrating an overall inorganic-rich SEI at both the inner and outer layers that stabilizes Li^+ transport. In contrast, NPSi electrodes show much lower LiF but higher organic components, demonstrating a thicker, organic, and phosphate-based SEI that lacks mechanical strength with higher impedance. In addition, it should be noted that the literature shows that carbon coating typically improves the electrochemical performance of the Si anode, as it affects the SEI chemistry,[60,61] which is worth studying in the future.

While we studied the effect of temperature on the electrochemical performance of the Si−C composite above, future studies should be carried out to explore how other deposition parameters, such as pressure, flow rate, and precursor concentration, influence the uniformity and electrochemical performance of Si−C composites. In addition, it is important to understand how the Si content influences electrochemical performance. We think the general trend is that a low Si content (e.g., <30%) will lead to a larger surface area and thus lower initial Coulombic efficiency, together with lower specific capacity, and a high Si content (e.g., >60%) will result in more volume expansion and cracks. The 40−45 wt % Si in our composite is suspected to be around optimal loading, but systematic studies should be performed to understand the dependence of electrochemical performance on Si content in the future.

We further analyze the specific energy of practical cells that can be achieved with the reported Si−C composite. Based on reasonable values in practical cells (Supporting Information Section S10), combining a Si−C composite anode (1400 mAh/g) and NMC cathode (200 mAh/g) can result in a cell-level specific energy of 366 Wh/kg under 4 mAh/cm^2 (Figure 5c). If instead graphite were used, the cell level specific energy would be 294 Wh/kg. Such high-capacity anodes approach the theoretically useful limit, with further improvements giving greatly diminished returns unless cathode capacities are improved, as shown in Figure 5c. For example, an anode capacity increase to 2500 mAh/g from 1400 mAh/g only translates to an increase of 4.4% at the cell-level to 382 Wh/kg. In contrast, a cathode improvement to 250 mAh/g with a 1400 mAh/g anode translates to an increase of 12.9% to 413 Wh/kg. Increasing the mass loading can similarly increase the overall specific capacity; for example, with a 1400 mAh/g anode and 7 mAh/cm^2 mass loading, specific energies of 386 Wh/kg and 440 Wh/kg can be achieved with 200 mAh/g and 250 mAh/g cathodes, respectively. Therefore, future work should focus on (1) the large-scale production of these materials, with emphasis on a simple and continuous product route for purified SiH_4, and (2) cathode improvements.

5. CONCLUSION

In comparison to other reported materials, the advantages of the micrometer-sized nanostructured Si−C composites are (1) compatibility with existing production methods for anodes. In essentially every aspect the material can be used as a drop-in replacement for graphite while tripling the specific capacity. (2) A straightforward production route at the laboratory scale via rotary-tube furnace CVD, enabling easy optimization of deposition uniformity and rate. Once optimized, the deposition parameters can readily be adapted to continuous, industrial-scale production methods such as fluidized bed CVD or concentric-tube designs.[62−64] (3) A relatively low production temperature of 480 °C with no external carbon coating required. (4) A low-cost and abundant precursor of porous carbon. In combination, this demonstrates that the material can reversibly deliver high capacity exceeding 1400 mAh/g, achieve high tapping density, high Si loading, and fast reaction kinetics, and prevent electrolyte incursion, all without compromising production scalability. If developments can be made in demonstrating the large-scale production of the materials, then it appears well-positioned to markedly increase the capacity of advanced Li-ion batteries, aiding in the progression toward a more sustainable world.

■ ASSOCIATED CONTENT

Data Availability Statement

All data are available in the manuscript or the Supporting Information. Information requests should be directed to the corresponding author.

Supporting Information

The Supporting Information is available free of charge at https://pubs.acs.org/doi/10.1021/acsanm.5c03801.

> Chemical vapor deposition setup, characterization of carbon particles and Si/C composite, SEM-EDS-FIB process, thermogravimetric analysis color change, cell fabrication details, Raman spectroscopy of Si-C composites, X-ray photoelectron spectroscopy performance of Si-C and NPSi anodes, and cell-level specific energy calculations and assumptions (PDF)

■ AUTHOR INFORMATION

Corresponding Author

Yuan Yang − *Department of Applied Physics and Applied Mathematics, Columbia University, New York, New York 10027, United States;* orcid.org/0000-0003-0264-2640; Email: yy2664@columbia.edu

Authors

Joseph F. Wild − *Department of Applied Physics and Applied Mathematics, Columbia University, New York, New York 10027, United States*

Yihan Li − *Department of Applied Physics and Applied Mathematics, Columbia University, New York, New York 10027, United States*

Yeshiyuan Zhou − *Department of Applied Physics and Applied Mathematics, Columbia University, New York, New York 10027, United States*

https://doi.org/10.1021/acsanm.5c03801
ACS Appl. Nano Mater. XXXX, XXX, XXX−XXX

Wenbo Bao − *Department of Applied Physics and Applied Mathematics, Columbia University, New York, New York 10027, United States*
Aishwarya Gujarathi − *Department of Applied Physics and Applied Mathematics, Columbia University, New York, New York 10027, United States*
Ruiwen Zhang − *Department of Applied Physics and Applied Mathematics, Columbia University, New York, New York 10027, United States*
Yuxuan Yang − *Department of Applied Physics and Applied Mathematics, Columbia University, New York, New York 10027, United States*
Tao Hu − *Gotion Inc, Fremont, California 94538, United States*
Taizhi Jiang − *Gotion Inc, Fremont, California 94538, United States*
Yihong Chen − *Gotion Inc, Fremont, California 94538, United States*

Complete contact information is available at: https://pubs.acs.org/10.1021/acsanm.5c03801

Author Contributions

J.F.W., Y.L., Y.Z., W.B., A.G., R.Z., and Yx.Y. performed the experiments and characterization. J.F.W. and Y.Y. wrote the manuscript. All authors contributed to data analysis. Y.Y. supervised the project.

Notes

The authors declare no competing financial interest.

■ ACKNOWLEDGMENTS

This work was supported by Gotion, Inc., USA.

■ REFERENCES

(1) Armand, M.; Tarascon, J. M. Building better batteries. *Nature* **2008**, *451*, 652−657.
(2) Scrosati, B.; Garche, J. Lithium batteries: Status, prospects and future. *J. Power Sources* **2010**, *195*, 2419−2430.
(3) Tarascon, J. M.; Armand, M. Issues and challenges facing rechargeable lithium batteries. *Nature* **2001**, *414*, 359−367.
(4) Zeng, S.; Duan, G.; Yu, R.; Qin, Q.; He, S.; Jiang, S.; Yang, H.; Han, X.; Han, J.; Xia, B. Y. Microstructure and bionic engineering of triphase reaction interface for zinc-air batteries. *Prog. Mater. Sci.* **2025**, *147*, 101356.
(5) Liu, Y.; Xiang, K.; Zhou, W.; Deng, W.; Zhu, H.; Chen, H. Investigations on Tunnel-Structure MnO_2 for Utilization as a High-Voltage and Long-Life Cathode Material in Aqueous Ammonium-Ion and Hybrid-Ion Batteries. *Small* **2024**, *20*, 2308741.
(6) Wen, X. Y.; Li, W.; Chen, H.; Zhou, W.; Xiang, K. X. $Zn_3V_3O_8$ nanorods with outstanding electrochemical kinetics as novel anode for aqueous ammonium-ion batteries. *Rare Met.* **2025**, *44*, 3881−3892.
(7) Guo, T.; Tang, L.; Deng, W.; Liu, G.; Zhou, W.; Wan, H.; Meng, L.; Chen, H. Cu_xO as an ultra-stable voltage plateaus and long-life cathode material in aqueous ammonium-ion batteries. *Rare Met.* **2025**, *44*, 4631−4641.
(8) Liang, A.; Dong, W.; Li, X.; Chen, X. A novel dual-mode paper fiber sensor based on laser-induced graphene and porous salt-ion for monitoring humidity and pressure of human. *Chem. Eng. J.* **2024**, *502*, 158184.
(9) Shang, Z.; An, X.; Nie, S.; Li, N.; Cao, H.; Cheng, Z.; Liu, H.; Ni, Y.; Liu, L. Design of B/N Co-doped micro/meso porous carbon electrodes from CNF/BNNS/ZIF-8 nanocomposites for advanced supercapacitors. *J. Bioresour. Bioprod.* **2023**, *8*, 292−305.
(10) An, W.; He, P.; Che, Z.; Xiao, C.; Guo, E.; Pang, C.; He, X.; Ren, J.; Yuan, G.; Du, N.; Yang, D.; Peng, D.-L.; Zhang, Q. Scalable Synthesis of Pore-Rich Si/C@C Core−Shell-Structured Microspheres for Practical Long-Life Lithium-Ion Battery Anodes. *ACS Appl. Mater. Interfaces* **2022**, *14*, 10308−10318.
(11) Dong, H.; Wang, J.; Ding, H.; Zong, F.; Wang, P.; Song, R.; Zhang, N.; Cui, X.; Cui, X.; Li, S. Exploring the practical applications of silicon anodes: a review of silicon-based composites for lithium-ion batteries. *Ionics* **2022**, *28*, 3057−3077.
(12) Ko, M.; Chae, S.; Ma, J.; Kim, N.; Lee, H. W.; Cui, Y.; Cho, J. Scalable synthesis of silicon-nanolayer-embedded graphite for high-energy lithium-ion batteries. *Nat. Energy* **2016**, *1*, 16113.
(13) Li, H.; Li, H.; Lai, Y.; Yang, Z.; Yang, Q.; Liu, Y.; Zheng, Z.; Liu, Y.; Sun, Y.; Zhong, B.; Wu, Z.; Guo, X. Revisiting the Preparation Progress of Nano-Structured Si Anodes toward Industrial Application from the Perspective of Cost and Scalability. *Adv. Energy Mater.* **2022**, *12*, 2102181.
(14) Liu, B.; Huang, P.; Xie, Z.; Huang, Q. Large-Scale Production of a Silicon Nanowire/Graphite Composites Anode via the CVD Method for High-Performance Lithium-Ion Batteries. *Energy Fuels* **2021**, *35*, 2758−2765.
(15) Liang, H.; Wang, R.; Fang, B.; Mo, R. Scalable engineering of porous micro-sized Si-C composites through direct conversion of CO_2 toward high-energy lithium-ion batteries. *J. Power Sources* **2025**, *652*, 237700.
(16) Yang, D.; Li, C.; Pan, L.; Chen, J.; Zhang, W.; Tian, Q. Dual modification of internal Co doping and surface Co nanoparticles decorating for boosting lithium storage of Si anode. *Chem. Eng. J.* **2025**, *513*, 162939.
(17) Xue, W.; Huang, M.; Li, Y.; Zhu, Y. G.; Gao, R.; Xiao, X.; Zhang, W.; Li, S.; Xu, G.; Yu, Y.; Li, P.; Lopez, J.; Yu, D.; Dong, Y.; Fan, W.; Shi, Z.; Xiong, R.; Sun, C. J.; Hwang, I.; Lee, W. K.; Shao-Horn, Y.; Johnson, J. A.; Li, J. Ultra-high-voltage Ni-rich layered cathodes in practical Li metal batteries enabled by a sulfonamide-based electrolyte. *Nat. Energy* **2021**, *6*, 495−505.
(18) Park, M. H.; Kim, M. G.; Joo, J.; Kim, K.; Kim, J.; Ahn, S.; Cui, Y.; Cho, J. Silicon Nanotube Battery Anodes. *Nano Lett.* **2009**, *9*, 3844−3847.
(19) Chan, C. K.; Peng, H.; Liu, G.; McIlwrath, K.; Zhang, X. F.; Huggins, R. A.; Cui, Y. High-performance lithium battery anodes using silicon nanowires. *Nat. Nanotechnol.* **2008**, *3*, 31−35.
(20) Liu, N.; Lu, Z.; Zhao, J.; McDowell, M. T.; Lee, H. W.; Zhao, W.; Cui, Y. A pomegranate-inspired nanoscale design for large-volume-change lithium battery anodes. *Nat. Nanotechnol.* **2014**, *9*, 187−192.
(21) Bourderau, S.; Brousse, T.; Schleich, D. M. Amorphous silicon as a possible anode material for Li-ion batteries. *J. Power Sources* **1999**, *81*, 233−236.
(22) Zhang, J. G.; Wang, W.; Xiao, J.; Xu, W.; Graff, G. L.; Yang, G.; Choi, D.; Wang, D.; Li, X.; Liu, J. Silicon-Based Anodes for Li-Ion Batteries. In *Encyclopedia of Sustainability Science and Technology*; SpringerLink, 2012; pp 9293−9316.
(23) Zhang, Y.; Wu, B.; Mu, G.; Ma, C.; Mu, D.; Wu, F. Recent progress and perspectives on silicon anode: Synthesis and prelithiation for LIBs energy storage. *J. Energy Chem.* **2022**, *64*, 615.
(24) Liu, X. H.; Zhong, L.; Huang, S.; Mao, S. X.; Zhu, T.; Huang, J. Y. Size-Dependent Fracture of Silicon Nanoparticles During Lithiation. *ACS Nano* **2012**, *6*, 1522−1531.
(25) McDowell, M. T.; Lee, S. W.; Harris, J. T.; Korgel, B. A.; Wang, C.; Nix, W. D.; Cui, Y. In Situ TEM of Two-Phase Lithiation of Amorphous Silicon Nanospheres. *Nano Lett.* **2013**, *13*, 758−764.
(26) Kwon, H. J.; Hwang, J. Y.; Shin, H. J.; Jeong, M. G.; Chung, K. Y.; Sun, Y. K.; Jung, H. G. Nano/Microstructured Silicon−Carbon Hybrid Composite Particles Fabricated with Corn Starch Biowaste as Anode Materials for Li-Ion Batteries. *Nano Lett.* **2020**, *20*, 625−635.
(27) Szczech, J. R.; Jin, S. Nanostructured silicon for high capacity lithium battery anodes. *Energy Environ. Sci.* **2011**, *4*, 56−72.
(28) Wu, M.; Sabisch, J. E. C.; Song, X.; Minor, A. M.; Battaglia, V. S.; Liu, G. In Situ Formed Si Nanoparticle Network with Micron-Sized Si Particles for Lithium-Ion Battery Anodes. *Nano Lett.* **2013**, *13*, 5397−5402.

(29) Xu, H.; Ding, M.; Li, D.; Liu, Y.; Jiang, Y.; Li, F.; Xue, B. Silicon nanoparticles coated with nanoporous carbon as a promising anode material for lithium ion batteries. *New J. Chem.* **2020**, *44*, 17323−17332.
(30) Lin, D.; Lu, Z.; Hsu, P. C.; Lee, H. R.; Liu, N.; Zhao, J.; Wang, H.; Liu, C.; Cui, Y. A high tap density secondary silicon particle anode fabricated by scalable mechanical pressing for lithium-ion batteries. *Energy Environ. Sci.* **2015**, *8*, 2371−2376.
(31) Shi, J.; Gao, H.; Hu, G.; Zhang, Q. Interfacial self-assembled Si@SiO_x@C microclusters with high tap density for high-performance Li-ion batteries. *Mater. Today Energy* **2022**, *29*, 101090.
(32) Wang, M.; Ma, Y.; Jiang, J.; Huang, Y.; Li, X.; Zheng, J.; Qin, C.; Yan, P.; Cao, G. Hierarchical Microspheres of Aggregated Silicon Nanoparticles with Nanometre Gaps as the Anode for Lithium-Ion Batteries with Excellent Cycling Stability. *ChemElectroChem* **2019**, *6*, 1139−1148.
(33) Hu, M.; Wu, H.; Zhang, G. J. High-performance silicon/graphite anode prepared by CVD using SiCl4 as precursor for Li-ion batteries. *Chem. Phys. Lett.* **2023**, *833*, 140917.
(34) Lee, C. Y.; Yeh, F. H.; Yu, I. S. A Commercial Carbonaceous Anode with a-Si Layers by Plasma Enhanced Chemical Vapor Deposition for Lithium Ion Batteries. *J. Compos. Sci.* **2020**, *4*, 72.
(35) Hoseini, S. A.; Mohajerzadeh, S.; Sanaee, Z. Flaky sputtered silicon MWCNTs core-shell structure as a freestanding binder-free electrode for lithium-ion battery. *Sci. Rep.* **2025**, *15*, 3733.
(36) Khanam, Z.; Luo, L.; Mushtaq, M.; Li, J.; Yang, H.; Ouyang, T.; Balogun, M. S.; Pan, A. Robust pseudocapacitive Na^+ intercalation induced by MoS_2 on active Mo_2C current collector interface for high areal capacity sodium-ion batteries. *Nano Energy* **2024**, *125*, 109590.
(37) Huang, S.; Yao, J.; Li, X.; Liu, H.; Qin, Y.; Wang, X.; Luo, D.; Shui, L. Tuning size and composition of Si/CNT composite microspheres via droplet-microfluidics for high performance lithium-ion batteries. *APL Mater.* **2024**, *12*, 011126.
(38) Kumankuma Sarpong, J.; Guo, W.; Fu, Y. Advances of Metal Oxide Composite Cathodes for Aqueous Zinc-Ion Batteries. *Adv. Energy Sustainability Res.* **2022**, *3*, 2100220.
(39) Luo, L.; Liang, K.; Khanam, Z.; Yao, X.; Mushtaq, M.; Ouyang, T.; Balogun, M. S.; Tong, Y. Monolithic Microparticles Facilitated Flower-Like TiO2 Nanowires for High Areal Capacity Flexible Li-Ion Batteries. *Small* **2024**, *20*, 2307103.
(40) Jung, M.; Park, J.; Lee, K.; Attia, N. F.; Oh, H. Effective synthesis route of renewable nanoporous carbon adsorbent for high energy gas storage and CO_2/N_2 selectivity. *Renewable Energy* **2020**, *161*, 30−42.
(41) Han, Z.; Wild, J. F.; Chen, J. J.; Yang, Y. Modeling Silane Deposition in Nanoporous Carbon for High-Capacity Si/C Composite Anodes. *Adv. Energy Sustainability Res.* **2024**, *5*, 0111.
(42) Onischuk, A. A.; Panfilov, V. N. Mechanism of thermal decomposition of silanes. *Russ. Chem. Rev.* **2001**, *70*, 321−332.
(43) Hong, W. E.; Ro, J. S. Kinetics of solid phase crystallization of amorphous silicon analyzed by Raman spectroscopy. *J. Appl. Phys.* **2013**, *114*, 073511.
(44) Koo, B.; Kim, H.; Cho, Y.; Lee, K. T.; Choi, N. S.; Cho, J. A highly cross-linked polymeric binder for high-performance silicon negative electrodes in lithium ion batteries. *Angew. Chem., Int. Ed.* **2012**, *51*, 8762−8767.
(45) Liu, Y.; Shao, R.; Jiang, R.; Song, X.; Jin, Z.; Sun, L. A review of existing and emerging binders for silicon anodic Li-ion batteries. *Nano Res.* **2023**, *16*, 6736−6752.
(46) Salah, M.; Pathirana, T.; de Eulate, E. A.; Hall, C.; Kerr, R.; Fabretto, M. Effect of vinylene carbonate electrolyte additive and battery cycling protocol on the electrochemical and cyclability performance of silicon thin-film anodes. *J. Energy Storage* **2022**, *46*, 103868.
(47) Xiao, Z.; Wu, H.; Quan, L.; Zeng, F.; Guo, R.; Ma, Z.; Chen, X.; Zhan, J.; Xu, K.; Xing, L.; Li, W. Micro-sized CVD-derived Si−C anodes: challenges, strategies, and prospects for next-generation high-energy lithium-ion batteries. *Energy Environ. Sci.* **2025**, *18*, 4037−4052.
(48) Chen, S.; Shen, L.; van Aken, P. A.; Maier, J.; Yu, Y. Dual-Functionalized Double Carbon Shells Coated Silicon Nanoparticles for High Performance Lithium-Ion Batteries. *Adv. Mater.* **2017**, *29*, 1605650.
(49) Choi, S.; Kwon, T.; Coskun, A.; Choi, J. W. Highly elastic binders integrating polyrotaxanes for silicon microparticle anodes in lithium ion batteries. *Science* **2017**, *357*, 279−283.
(50) Domi, Y.; Usui, H.; Okasaka, T.; Nishikawa, K.; Sakaguchi, H. Silicon-Based Nanocomposite Anodes with Excellent Cycle Life for Lithium-Ion Batteries Achieved by the Synergistic Effect of Two Silicides. *J. Electrochem. Soc.* **2024**, *171*, 080506.
(51) Domi, Y.; Usui, H.; Sakaguchi, H. Analysis of the interfacial reaction between Si-based anodes and electrolytes in Li-ion batteries. *Chem. Commun.* **2024**, *60*, 12986.
(52) Hu, T.; Zhou, H.; Tang, J.; Chen, S.; Li, Z.; Yu, X.; Zhang, Y.; Yang, J.; Zhou, X. Stable lithium storage with strong-grain sustained pinning-reinforced nanocrystalline silicon. *Energy Environ. Sci.* **2024**, *17*, 6377−6392.
(53) Jia, H.; Li, X.; Song, J.; Zhang, X.; Luo, L.; He, Y.; Li, B.; Cai, Y.; Hu, S.; Xiao, X.; Wang, C.; Rosso, K. M.; Yi, R.; Patel, R.; Zhang, J.-G. Hierarchical porous silicon structures with extraordinary mechanical strength as high-performance lithium-ion battery anodes. *Nat. Commun.* **2020**, *11*, 1474.
(54) Kimura, Y.; Domi, Y.; Usui, H.; Sakaguchi, H. Improved Cycling Performance of $Cr_xV_{1-x}Si_2$/Si Composite Electrode for Application to Lithium-Ion Battery Anodes. *J. Electrochem. Soc.* **2022**, *169*, 010537.
(55) Qin, X.; Zhao, L.; Han, J.; Xiao, J.; Wang, Y.; Ji, C.; Liu, T.; Zuo, M.; Sun, J.; Kong, D.; Wu, M.; Lv, W.; Yang, Q.-H.; Zhi, L. Self-Pressure Silicon−Carbon Anodes for Low-External-Pressure Solid-State Li-Ion Batteries. *ACS Nano* **2025**, *19*, 17760−17773.
(56) Wang, H.; Fu, J.; Wang, C.; Wang, J.; Yang, A.; Li, C.; Sun, Q.; Cui, Y.; Li, H. A binder-free high silicon content flexible anode for Li-ion batteries. *Energy Environ. Sci.* **2020**, *13*, 848−858.
(57) Wang, Q.; Zhu, M.; Chen, G.; Dudko, N.; Li, Y.; Liu, H.; Shi, L.; Wu, G.; Zhang, D. High-Performance Microsized Si Anodes for Lithium-Ion Batteries: Insights into the Polymer Configuration Conversion Mechanism. *Adv. Mater.* **2022**, *34*, 2109658.
(58) Yan, W.; Mu, Z.; Wang, Z.; Huang, Y.; Wu, D.; Lu, P.; Lu, J.; Xu, J.; Wu, Y.; Ma, T.; Yang, M.; Zhu, X.; Xia, Y.; Shi, S.; Chen, L.; Li, H.; Wu, F. Hard-carbon-stabilized Li−Si anodes for high-performance all-solid-state Li-ion batteries. *Nat. Energy* **2023**, *8*, 800−813.
(59) Chen, Y.; Tian, Z.; Li, J.; Zhou, T. In-situ constructing pearl necklace-shaped heterostructure: Zn^{2+} substituted $Na_3V_2(PO_4)_3$ attached on carbon nano fibers with high performance for half and full Na ion cells. *Chem. Eng. J.* **2023**, *472*, 145041.
(60) Müller, J.; Abdollahifar, M.; Doose, S.; Michalowski, P.; Wu, N.; Kwade, A. Effects of carbon coating on calendered nano-silicon graphite composite anodes of LiB. *J. Power Sources* **2022**, *548*, 232000.
(61) Hernandha, R.; Rath, P.; Umesh, B.; Patra, J.; Huang, C.; Wu, W.; Dong, Q.; Li, J.; Chang, J. Supercritical CO2-Assisted SiO_x/Carbon Multi-Layer Coating on Si Anode for Lithium-Ion Batteries. *Adv. Funct. Mater.* **2021**, *31*, 2104135.
(62) Coppey, N.; Noé, L.; Monthioux, M.; Caussat, B. Fluidized bed chemical vapor deposition of silicon on carbon nanotubes for Li-ion batteries. *J. Nanosci. Nanotechnol.* **2011**, *11*, 8392−8395.
(63) Yang, J.; Kahn, H.; He, A.-Q.; Phillips, S. M.; Heuer, A. H. A new technique for producing large-area as-deposited zero-stress LPCVD polysilicon films: the MultiPoly process. *J. Microelectromech. Syst.* **2000**, *9*, 485−494.
(64) Song, H.; Zhang, X.; Ye, J.; Yang, Y.; Sun, D.; Xu, C.; Lin, R.; Zhang, X.; Zhang, M.; Li, S.; Gao, J.; Xu, J.; Ma, X.; Li, Y. Si@Graphene composite anode with high capacity and energy density by fluidized chemical vapor deposition. *Chem. Eng. Sci.* **2023**, *274*, 118706.

https://doi.org/10.1021/acsanm.5c03801
ACS Appl. Nano Mater. XXXX, XXX, XXX−XXX